ELSEVIER

Mechanics of Materials 33 (2001) 573–591

MECHANICS OF MATERIALS

www.elsevier.com/locate/mechmat

The role of thermal activation on dynamic stress-induced inelasticity and damage in Ti–6Al–4V

H.V. Arrieta, H.D. Espinosa *,[1]

School of Aeronautics and Astronautics, Purdue University, West Lafayette, IN 47907-1282, USA

Received 28 September 2000; received in revised form 27 July 2001

Abstract

Planar impact experiments are performed on preheated Ti–6Al–4V specimens, at temperatures in the range 25–550 °C, to determine the role of thermal activation on dynamic stress-induced inelasticity and damage. Measurements in this high temperature and high strain rate regime are made possible by modification of the standard plate impact facility to include heating capabilities. This paper describes in detail needed hardware and experimental procedure. A symmetric planar impact configuration is employed to achieve high compressive and tensile stresses in the specimens. The targets are heated by a magnetic field generated by current flow on a coil surrounding the specimen. Interferometric techniques are employed to record the free surface velocity of the target plates. The experimental results show that thermal activation overcomes the role of rate dependence in the material constitutive behavior. The Hugoniot elastic limit (HEL) and spall strength of Ti–6Al–4V significantly decrease with temperature despite the high strain rate, about 10^5 s^{-1}, used in the tests. The damage mechanism remains the same at high and room temperatures, i.e., microvoid nucleation, growth and coalescence. Microscopy studies, performed on recovered samples, show that temperature substantially reduces the strain inhomogeneity leading to microvoid formation and that a change in void nucleation site occurs. A completely reversible shock-induced phase transformation $\alpha \rightarrow \omega$ appears to be present in the tested Ti–6Al–4V. Evidence of this phase transformation is observed in the velocity histories upon unloading of the first compressive pulse. The phase transformation is controlled by a combination of thermal and stress driven mechanisms. © 2001 Published by Elsevier Science Ltd.

Keywords: Dynamic plasticity; Damage; Spallation; Failure mechanisms; High temperature testing; Phase transformation

1. Introduction

Understanding material response at high temperatures and high strain rates is essential to the development of models describing dynamic failure of advanced materials. Such models are of crucial importance to many applications. For instance, crack arrest in engineering structures, failure of turbine engine blades, foreign object impact on satellites and aircrafts, automotive crashworthiness and military applications such as projectile deformation and armor penetration. Our current understanding of basic properties like plastic flow or dynamic fracture strength in the high temperature and high strain rate regime is very limited.

* Corresponding author. Tel.: +1-847-4675989; fax: +1-847-4913540.

E-mail address: espinosa@nwu.edu *URL:* http://www.mech.nwu.edu/~espinosa (H.D. Espinosa).

[1] Present address: Department of Mechanical Engineering, Northwestern University, 2145 Sheridan Rd., Evanston, IL 60208-3111, USA.

0167-6636/01/$ - see front matter © 2001 Published by Elsevier Science Ltd.
PII: S0167-6636(01)00079-5

This is the case because of the scarcity of experimental studies with the needed spatial and temporal resolution to identify damage and failure mechanisms.

Plate impact experiments offer unique capabilities for the dynamic characterization of advanced materials. The stress amplitudes and deformation rates obtained in these experiments allow the identification of damage and material instabilities (Espinosa and Nemat-Nasser, 2000). One-dimensional strain waves, in the central region of the specimen, allow a clear interpretation of experimental results, see also Clifton (1971).

In most engineering materials, damage and inelasticity is governed by atomistic mechanisms. For instance, plastic deformation is controlled, at an atomic level, by obstacles like line and point defects or second phases. More than 60 years ago, the importance of thermal energy in assisting the applied stress to overcome these obstacles was realized. By contrast, other sources of inelasticity such as twining are essentially athermal and solely driven by the stress field. The competition between these inelastic mechanisms determines the overall response of the material. A correlation of microstructural features associated with the information gathered from impact experiments can lead to more accurate damage and failure models.

It is known that high strain rates increase the yield stress in metals (Yadav and Ramesh, 1995; Chiem and Duffy, 1983; Nemat-Nasser and Guo, 2000), whereas it is generally accepted that a rise in temperature tends to reduce the resistance to flow by lowering activation barriers associated with the atomic mechanisms of deformation, see Johnson (1979), Campbell (1973) and Hirschvogel (1978). When a metallic material is subjected to dynamic and high temperature loading, a competition between work hardening (resulting from the production, motion and interaction of dislocations and other defects) and thermal softening occurs. Extensive research into the identification of stress–strain curves as a function of temperature was carried out by Zhou and Baker (1994) and Sakai et al. (1988) for many b.c.c and f.c.c metals. These results show that temperature has a much greater effect on material strength than strain rate if the deformation is performed under both high strain rate and high temperature conditions.

The binary titanium alloy, Ti–6Al–4V, was chosen for this study due to its relevance to the applications previously discussed. Its excellent strength-to-weight ratio, which is maintained at elevated temperature, and fracture resistance make this alloy very attractive to aerospace applications, see Wood (1972), Donachie (1988), and Collings and Ho (1970). Understanding its dynamic damage evolution, under elevated temperatures, would lead to optimum usage of Ti–6Al–4V in turbine blades, armor plates and many other structural components. The dynamic behavior of Ti–6Al–4V at room temperature has been characterized by Follansbee and Gray III (1989), Meyer (1984) and Me-Bar et al. (1987). From their studies a general dynamic behavior emerges for Ti–6Al–4V; high strength, strain hardening, appreciable rate sensitivity, negligible strain rate history effects and spall strength almost insensitive to microstructural changes.

Some studies on Ti–6Al–4V under elevated temperature and high strain rate have been recently reported by Lee and Lin (1997, 1998). These studies were performed in a Hopkinson bar apparatus at strain rates in the range 5×10^2–3×10^3 s^{-1} and temperatures in the range 22–1200 °C. It was found that the polymorphic transformation the alloy undergoes, in the tested range, appears not to play an important role in its constitutive behavior. However, the role of inelasticity and damage on material behavior at elevated temperatures and strain rates needs further investigation.

Even though damage mechanisms at high strain rates are not completely understood, researchers agree that the Hugoniot elastic limit (HEL) corresponds to the onset of material inelasticity under one-dimensional strain conditions. Hence, the evolution of the HEL or its equivalent, the dynamic yield stress, with temperature is crucial to define and model material inelasticity. Under one-dimensional strain condition, the dynamic fracture process leading to failure, is also known as spallation. The spall process in ductile metals is governed by simultaneous nucleation, growth, and coalescence of microvoids or microcracks that

form a failed or spalled region. Thermal energy plays an important role in the deformation mechanisms leading to strain inhomogeneities that drive the microvoid formation process. Limited experimental work exists about the role of thermal activation on spall behavior of materials. Recently, work by Kanel et al. (1996) and Golubev and Sobolev (1999) on aluminum and magnesium was published. These investigators found that spall strength drops with temperature, but no further investigation was carried out to establish the role of the microstructure in the spallation process.

This paper describes the experimental technique developed for shock impact testing at high temperature and report the variation of HEL and spallation with temperature in Ti–6Al–4V. Microstructural analyses that provide insight into the deformation mechanisms of the shocked material is also reported.

2. Experimental technique

Our dynamic inelasticity laboratory posses an experimental facility to perform planar impact experiments at different temperatures. The setup is similar to the one developed by Frustchy and Clifton (1998) for pressure–shear impact experiments. These capabilities broaden the range of achievable strain rates and temperatures, as shown in Fig. 1. The very high temporal resolution required to identify material inelasticity is achieved by means of an air-delay leg velocity interferometer capable of measuring normal free surface velocity under a wide range of temperatures.

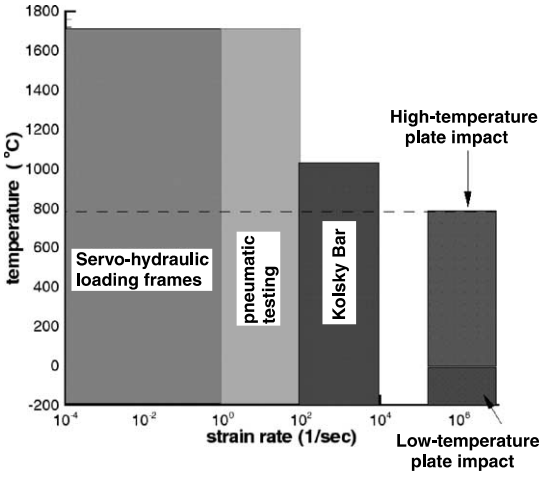

Fig. 1. Material testing techniques as a function of strain rate and temperature.

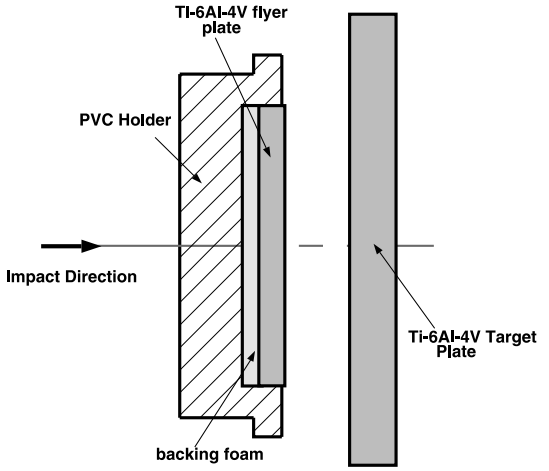

Fig. 2. High temperature experimental configuration.

The selected experimental configuration is a symmetric planar impact or spall experiment, see Fig. 2. The elastic wave fronts and their interaction are easily understood by examining the time–distance (t–X) Lagrangian diagram shown in Fig. 3. At impact, plane compression waves are produced in both the flyer and the specimen (state 1). The reflection from the foam-flyer interface unloads, almost completely, the compressive wave resulting in a compressive pulse duration equal to the round

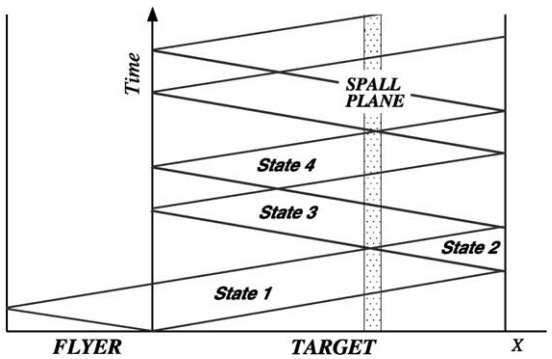

Fig. 3. Lagrangian X–t diagram for a symmetric impact.

trip travel time through the flyer thickness. When the compressive pulse reaches the rear surface of the specimen, a reflected wave is generated. This wave unloads the compressive pulse (state 2). Tensile stresses are generated when the two unloading waves, one from the flyer and the other from the specimen back surface, meet in the central part of the specimen (state 3). This location is named the spall plane and it is where the target is expected to fail. By the time the tensile pulse reaches the flyer-specimen interface, separation takes place and the pulse reflection causes compressive stresses (state 4). For the reported experiments, the thickness of the targets is close to 8 mm for all specimens with a corresponding half thickness for the flyers. In this way, the spall plane is located near the middle of the target.

Clifton (1971) has developed the elastic–plastic solution to this wave propagation problem and showed that the stress level at the spall plane depends only on the impact velocity V_1 when flyer and target are made of the same material. The testing velocity range was selected such that the lowest velocity is enough to induce dynamic yield in Ti–6Al–4V, about 900 MPa according to Wood (1972), whereas the highest velocity would induce spallation. Elastic wave propagation theory provides a reference for inferring inelastic behavior. In fact, any variation from this solution is caused by inelastic mechanisms such a plasticity and/or damage.

2.1. Experimental facility

The experiments were conducted in our dynamic inelasticity laboratory. This facility consists of a smooth bore 3 in. gas gun, for impacting different target materials at a prescribed velocity, external hardware to heat up the samples and an interferometric system for recording the wave profiles.

The gas gun facility has four interconnected parts: a pressure chamber or breech, a gun barrel, a target chamber and a catcher tank, see Fig. 4. The gun has a wrap around breech which employs no moving parts under pressure except the projectile itself as a fast-opening valve. The barrel inner surface is mirror polished to reduce friction, and a key-way, all the way through, guide the projectile without rotation. The target chamber is equipped with a special mounting system to hold the target assembly. This system allows remote rotation of the target, in any direction, to preserve alignment upon target heating. Prior to the experiment, the chamber and gun barrel are evacuated, to a pressure of approximately 50 mT, to

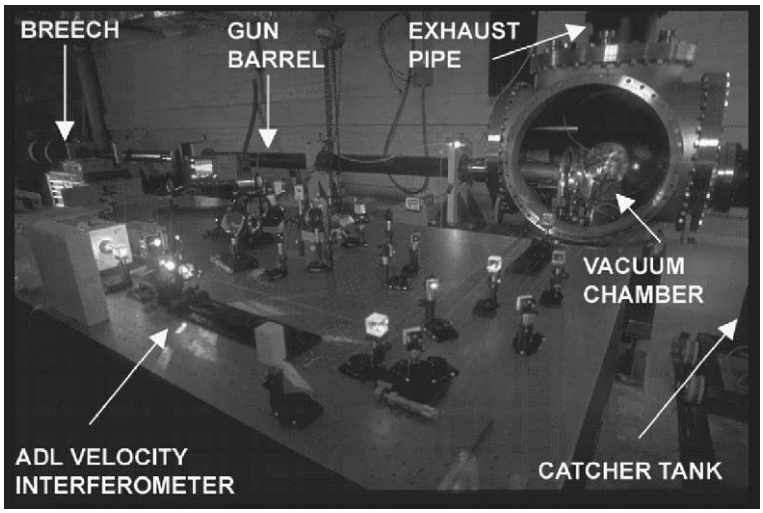

Fig. 4. Gas gun facility: breech, barrel, vacuum chamber, exhaust pipe, catcher tank and optical table with ADL velocity interferometer are shown.

prevent the formation of an air cushion between the target and flyer at impact. The vacuum is achieved by means of two vacuum pumps, operating in parallel, and a liquid nitrogen cold trap. To avoid overpressure in the target chamber, after impact, an exhaust system to ambient air has been implemented, see Fig. 4. The target and specimen leave the vacuum chamber through a rear port. A catcher tank filled with cotton rugs is used to decelerate and recover the projectile and target plates.

To perform plate impact experiments at elevated temperatures, external hardware was added. The high temperature facility consists of a high frequency (0.5 MHz) induction heating system STATION POWER LSP12 (25 kW) from LEPEL. Temperatures up to 1200 °C in metallic and ceramic materials have been achieved in calibration tests. A schematic of the high temperature target assembly can be seen in Fig. 5. The induction copper coil is mounted in the mentioned target holder and connected to the heating system by means of a specially designed feedthrough. The coil is made from copper tubing. The copper section conducts the high frequency electrical energy, whereas the inner core carries refrigeration water. The intense electromagnetic field inside the coil induces parasite currents in the magnetic target. A graphite susceptor holder is employed to keep in place the target, whereas a ceramic sleeve is placed between the sample and the copper coil to confine the heat to the sample. A copper shield, with circulating water, is superimposed to reduce heat transfer to the chamber environment and isolate electromagnetic radiation. A picture of the described system can be seen in Fig. 6.

2.2. Tested material

Hot-rolled plates of Ti–6Al–4V, provided by Dr. Wells from the Army Research Laboratory, were used in this investigation. The complete

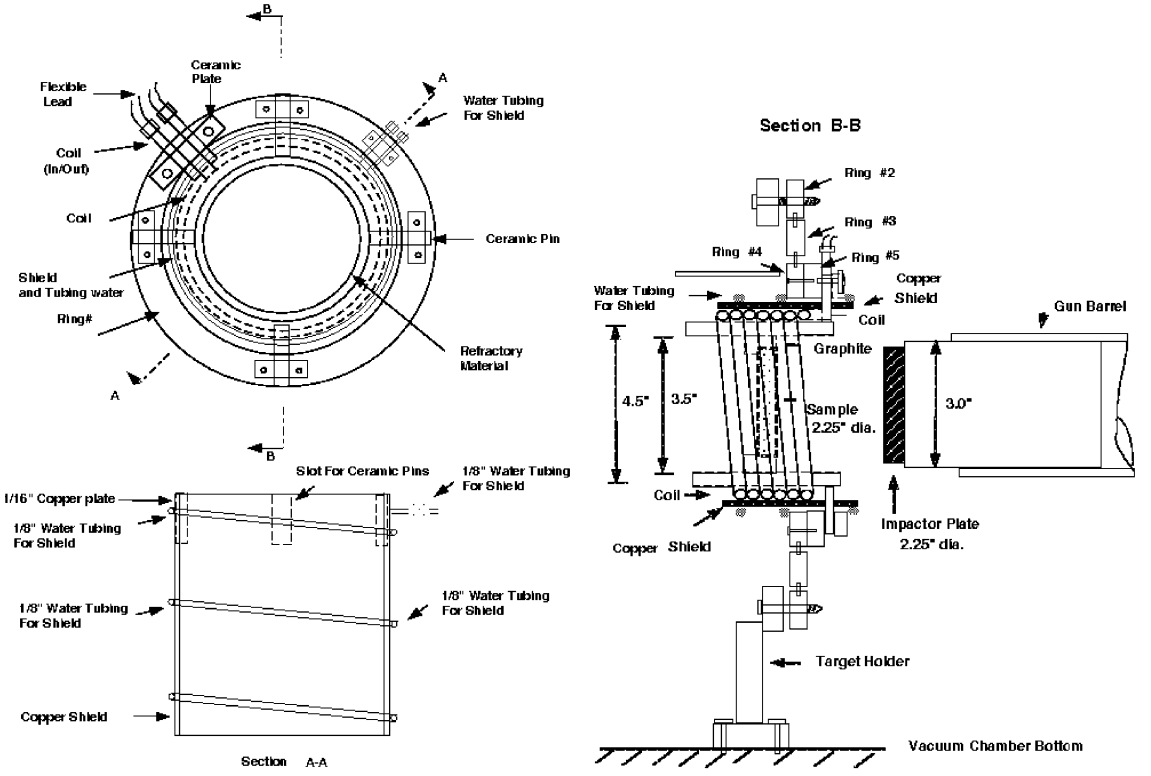

Fig. 5. High temperature system: front, top and side views.

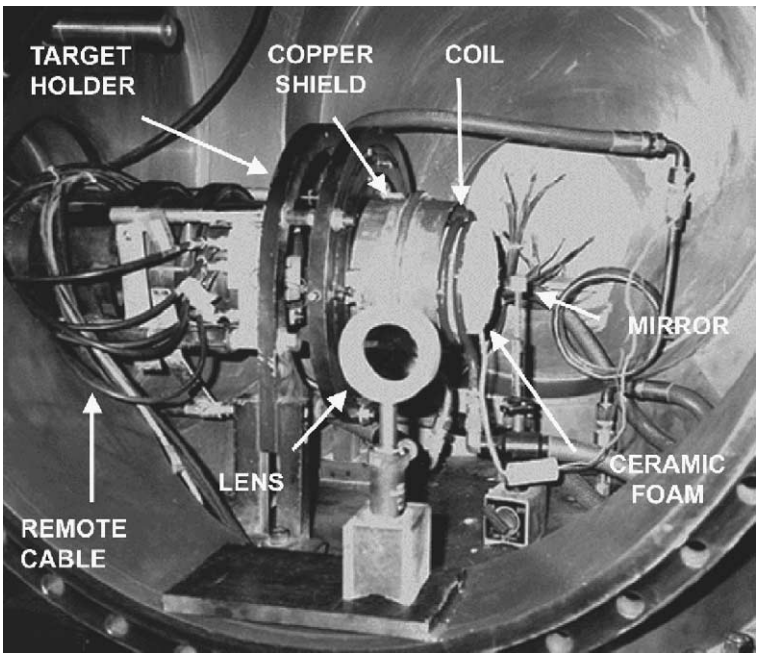

Fig. 6. Photograph of high temperature target assembly.

processing consisted in the generation of single melt ingots by means of electron beam melting. The ingot surface was machined and rolled to 8.25 in. slabs from 2100 °F. Then they were cut into three sections and reheated to 1725 °F, and rolled to 1 in. thick plates. The plates were subsequently annealed at 1725 °F for 2 h, roller leveled and annealed at 1400 °F for 1 h. Finishing was done by overall belt grinding. No additional heat treatment was performed prior to testing.

A metallographic examination showed that the starting material had a microstructure consisting of equiaxed and acicular α-phase (90%) and a small amount of intergranular β-phase (10%), see Fig. 7. The nominal α grain size varied from 8–15 μm with and aspect ratio of 2–10. The β-grain size was less homogeneous with a grain size varying from 5–20 μm. It was also possible to observe that acicular β-phase is oriented in the rolling direction. The described microstructure is typical of annealing followed by a hot-roll processing (Donachie, 1988). The target and flyer plates were all machined from the provided plates in such a way that the impact axis was perpendicular to the rolling direction. The hardness was measured to be 35.6 RC. At room temperature, the longitudinal wave speed, ultrasonically measured, was $c_L = 6232$ m/s and the material density was 4430 kg/m^3. Hence, the acoustic impedance of the alloy is 27.608 GPa/mm/μs. The chemical composition of the as-received plates is shown in Table 1. It should be noticed that the high interstitial oxygen content is 0.18%.

2.3. Experimental procedure

The experimental procedure shares several common features with the normal impact and pressure–shear experiments described in Espinosa and Clifton (1991). The projectile used for these experiments consists of a fiberglass tube, approximately 20 cm long, with an aluminum back piston on the rear end and a PVC holder with the flyer plate at the front. The fiberglass tube is machined to slide smoothly in the gun barrel with a radial tolerance of 30 μm. A small orifice in the fiberglass tube ensures that the pressure inside the projectile remains essentially the same as that outside to

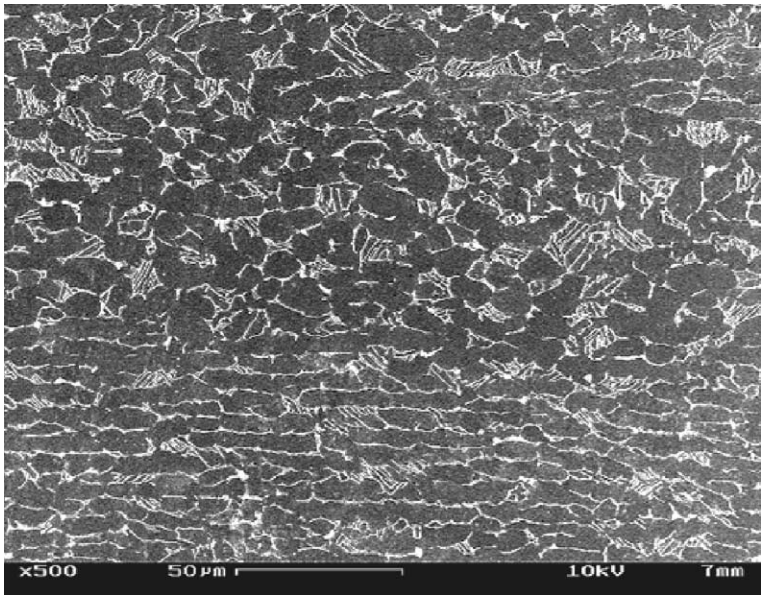

Fig. 7. Micrograph of Ti–6Al–4V as received, α-phase is gray and β-phase is white.

prevent unwanted deformation of the flyer plate when the system is under vacuum. The aluminum back piston is screwed to the fiberglass and holds two o-rings to seal the gas present in the wrap around breech. A plastic key that fits in the barrel key-way is placed in a special slot of the projectile to prevent its rotation, see Fig. 8. The PVC holder carries the titanium flyer backed by a soft foam on the projectile front end. All the pieces are glued together with 5 min epoxy.

The Ti–6Al–4V sample is placed hand tight inside the graphite susceptor, and glued with high temperature glue. The two pieces are slipped together into the ceramic sleeve and firmly attached by high temperature glue and ceramic pins that go all the way through the sleeve, see Fig. 8.

The induction heating process generates a temperature gradient in the sample. The induced currents tend to stay at the surface of the specimen generating more heat at the surface than in the bulk of the material (Chen and Ahrens, 1998). Titanium alloys have low thermal conductivity, therefore the heating gradient can be important. A

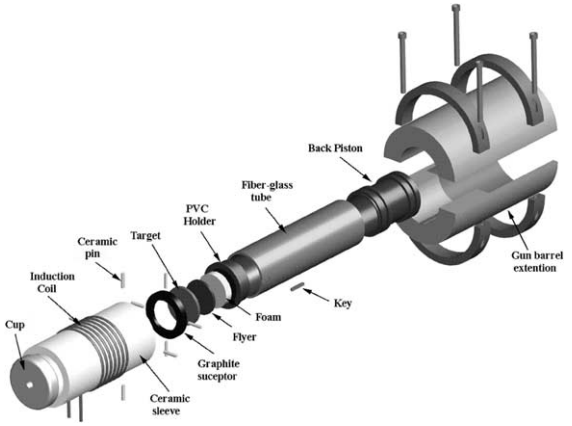

Fig. 8. Exploded view of projectile and target assembly. The copper shield, alignment rings and velocity system are not shown.

Table 1
Chemical composition of tested Ti–6Al–4V (in wt%)

Al	V	O	Fe	C	N	H
6.1%	4.0%	0.18%	0.2%	0.014%	0.008%	0.0057%

reduction in the coil diameter generates denser electromagnetic field that can penetrate the shield generated by the induced currents achieving a more homogeneous heating (Chen and Ahrens, 1998). A more practical approach is to employ a material with high electrical conductivity and heat thermal capacity, to hold the target. This configuration allows a reasonable time for temperature homogenization. The graphite susceptor shown in Fig. 8 is introduced in the developed setup with this aim. Temperature is measured by a thermocouple attached to the rear surface of the specimen, as close as possible to the center point.

The high velocities required in this study generate a strong shock-wave upon the firing of the projectile from the launch tube. To protect the high temperature assembly, an extension is added to the gun barrel. Following aerodynamic considerations, the extension was designed to keep the high temperature target assembly outside of an 18° cone. An explode view of the described experimental assembly is shown in Fig. 8.

The plates are first optically aligned at room temperature using the technique described by Kumar and Clifton (1976). This technique ensures the faces of the flyer and the specimen are aligned parallel to an accuracy of 2.0×10^{-5} radians. To correct the tilt generated during the heating process, a remote target alignment technique similar to the one described by Frustchy and Clifton (1998) is employed. Before the projectile is pulled back to the other end of the launch tube, a collimated laser beam reflected from the rear surface of the target plate is monitored on a stationary screen roughly 8 m away. A target plate tilt of 1 milliradian results in a beam translation of 1.2 cm on this screen. At elevated temperature, remote cables connected to the target holders, see Fig. 6, allow the alignment beam to be brought back to its original position, thereby ensuring that the target and the flyer plates maintain their original room temperature alignment. The quality of the interferometric signals, during the experiments, shows that the desired parallelism is preserved.

The velocity of the projectile just prior to impact is measured by means of a method that is similar to the one described by Fowles (1970). Five pins of constantan wire are set at the exit of the gun barrel. When the projectile shorts the voltage biased pins to ground an oscilloscope records the time intervals acquired by an electronic circuit. The distance between the pins, measured with a traveling microscope possessing μm accuracy, is then divided by these time intervals to compute projectile velocity. The accuracy of the system is better than 1%.

A disposable mirror is placed at a certain distance from the rear face of the specimen to reflect the beam used in the velocity interferometer. The motion of the rear surface of the specimen is then monitored in real time. The target chamber has a side window to provide access for the laser beam that is used in the ADL velocity interferometer depicted in Fig. 9. The interferometer fringe pattern and velocity are recorded by two digital oscilloscopes, LeCroy 9384L and Tektronix TDS520C2M, with maximum sample rate up to 4 Gs/s, 1 GHz bandwidth and 8 MB memory. The oscilloscopes are employed at full bandwidth and with a sample rate of 1 Gs/s. To avoid overheating of the mirror employed to collect laser light, a ceramic cup is used to close the ceramic sleeve that contains the target, see Fig. 8. A small hole is drilled on the center of the cup and the laser light is sent in and out through it.

2.3.1. Specimen preparation

In order to ensure that plane waves are generated at impact, the faces of the flyer plate and specimen must be essentially flat. The flyer plate and specimen are lapped flat using a 24 in. lapping machine with a cast iron lapping plate and 20 μm SiC powder suspended in a four-to-one water–oil solution. The flatness is checked by means of an optical flat glass and monochromatic light ($\lambda = 587.6$ nm). Once the flatness is acceptable, less than two Newton's rings, the plates are cleaned ultrasonically in MEK, acetone and methanol in that order. Then, the two plates are polished on a Texmet cloth sheet using 6, 3, 1 μm diamond paste, and 0.3 μm alumina slurry up to a mirror-polished surface. This finish is essential for an easy flyer-specimen alignment and good recording of velocity signals.

Titanium is a highly reactive material that oxidizes very fast. Thin oxide films are formed in ti-

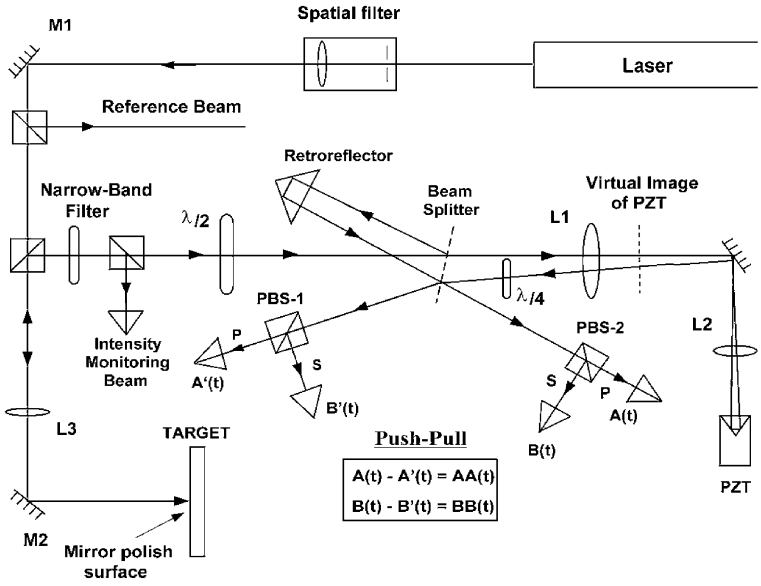

Fig. 9. Air delay leg (ADL) velocity interferometer.

tanium alloys at temperatures between 315 and 650 °C. Due to the high surface temperature generated by the induction heating method, which can reach 600 °C, an oxide layer usually forms even under vacuum. This oxide layer reduces the reflectivity of the target compromising the signal-to-noise ratio in the interferometer. To overcome this difficulty, a 0.1 μm thick platinum coating is applied on the back surface of the specimen. Platinum is stable at high temperature; however, an allotropic transformation of the Ti–6Al–4V at 955 °C increases its diffusion rate by 10 times. Therefore, the platinum coating may slowly defuse into the titanium alloy plate. Trial and error established a maximum exposure time, at the experimental conditions, to be approximately 20–30 min before interferometric signal deterioration. This time was enough for final checking of signal strength and for conducting the test.

2.4. Experimental results and discussions

A summary of performed impact experiments is presented in Table 2. A first experiment, 98-0924, was performed to have a reference material behavior at room temperature. Its time–velocity history is shown in Fig. 10. The elastic precursor is lost due to the low velocity per fringe (18.75 m/s) employed in the interferometer. 12 fringes are added to the fringe count to match the boundary conditions, see Barker (1972). The velocity jump corresponding to the HEL is 200.5 m/s, in good agreement with 201± m/s reported by Brar and Hopkins (1999).

Table 2
Summary of experimental parameters

Shot no.	Impactor thickness (mm)	Target thickness (mm)	Impact velocity (m/s)	Normal stress (GPa)	Preheated temperature (°C)
98-0924	3.60	7.6	251	3.46	22
98-1210	3.51	7.79	272	3.57	298
99-0602	3.54	7.62	417	5.45	315
99-1008	3.58	7.61	594	7.45	513

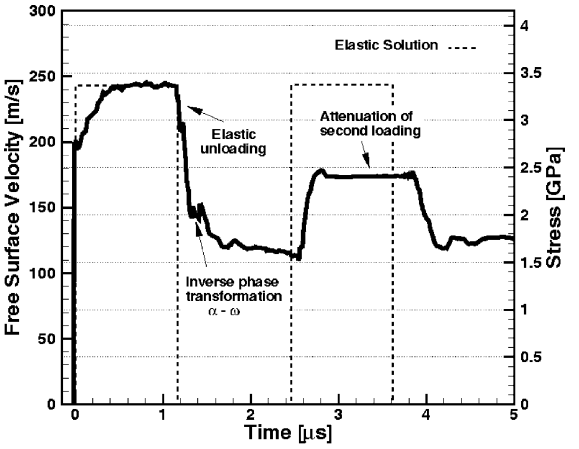

Fig. 10. Surface velocity history for experiment 99-0924, temperature 22 °C, $V_0 = 251$ m/s.

The transition between elastic to plastic behavior in unloading is clearly captured. There is a sharp elastic unloading followed by a dispersive unloading tail. The dispersion in unloading is mainly due to plastic deformation and tensile damage. The reloading pulse, that is generated by pulse reflection at the flyer-specimen interface, is greatly reduced with respect to the expected elastic behavior. Even though some hardening is expected due to the passage of the first loading pulse, the hardening must appear as a change in the slope of the second loading pulse instead of the observed attenuation. The attenuation indicates that part of the energy is dissipated in the form of shock-induced damage at the applied stress level. Note that no pull-back signal is observed in the free surface velocity record. Hence, the stress pulse attenuation is indicative of damage initiation without the formation of a spall plane within the sample.

An interesting feature of experiment 99-0924 is the oscillation of the velocity profile close to the end of the first unloading. Pure titanium is known to have metastable high temperature ω-phase (Sikka et al., 1982). The presence of ω-phase leads to an increase in hardness with consequent loss of ductility. Sikka et al. found that the ω-phase in titanium reverts back to equilibrium phases during high temperature aging and during plastic deformation. Vohra et al. (1977) discovered that the ω-start pressure varies from 2.2 to 6.0 GPa., depending on oxygen content and other interstitial elements. In addition, Gray III (1998) found evidence of a shock-induced phase transition, $\alpha \rightarrow \omega$, in high purity titanium at a stress level of 10.4 GPa. The $\alpha \rightarrow \omega$ phase transformation is consistent with a diffusionless displacive transition (Sikka et al., 1982). Moreover, a reduction in slip deformation and an increase in twining is known to lead to the $\alpha \rightarrow \omega$ transformation (Song and Gray III, 1994). Shock-wave loading of Ti–6Al–4V at room temperature was found to induce significant activation of deformation twining, whereas a substructure consisting of planar slip is activated at low strain rates (Gray III and Morris, 1989). Mescheryakov et al. (1999) reported that oscillations in their VISAR signal appears to indicate a shock-induced phase transformation in Ti–6Al–4V. Their post-test SEM studies, performed over samples recovered right after the experiment, in a water chamber, presented evidence of a ω residual phase in the microstructure. Our experimental setup does not allow us to cool down the samples right after impact, but the similarity with Mescheryakov et al. (1999) in the interferometric records suggests the existence of a shock-induced phase transformation in the tested Ti–6Al–4V. The stress level for the transformation is 2.17 GPa, close to ω-start pressure reported by Vohra et al. (1977), but lower than the phase transition reported by Mescheryako, 2.95 GPa. The direct $\alpha \rightarrow \omega$ transformation is not observed in the velocity history because it is overcome by the elastic wave.

A second experiment 98-1210 was performed with the purpose to compare the effect of temperature on damage kinetics at similar stress levels. The elastic precursor is also lost in this experiment, 12 fringes are added to match boundary conditions. A higher plastic deformation expected at high temperature, makes the slope of the plastic wave more pronounced, as can be observed in Fig. 11 . The smoothness of the velocity profile shows a progressive deformation of the free surface, clear indication of high plastic deformation. The velocity jump corresponding to the HEL is 166 m/s, which is smaller than the one measured at room temperature. This shows a decrease in dynamic yield stress with temperature. The so-called

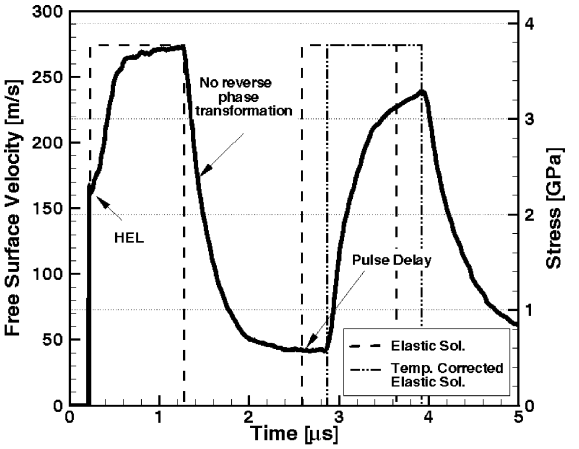

Fig. 11. Surface velocity history for experiment 98-1210, temperature 298 °C, $V_0 = 272$ m/s.

precursor decay is also more pronounced due to the increased rate of plastic deformation.

A delay in the second compressive pulse appears if room temperature elastic properties are used for calculating the elastic solution. Using temperature corrected elastic constants, see Fukuhara and Sanpei (1993), to calculate the wave propagation velocity, a good match with the elastic solution is achieved. During an impact experiment part of plastic work transforms into heat adiabatically, hence the heat builds up raising the material temperature. It is interesting to compare the final temperature rise with the β-transus temperature to account for possible allotropic phase transformations. In this last experiment the temperature rise was estimated in only 17 °C, giving a final temperature of 315 °C well below the β-transus temperature range for Ti–6Al–4V, which is 570–650 °C.

No evidence of shock-induced phase transition appears in this experiment, see first unloading in Fig. 11. A possible explanation is the type of dominant deformation mechanisms at the tested temperatures. Slip deformation is a thermal activated mechanism (Hertzberg, 1996), and therefore it is favored at high values of homologous temperature. The increase in slip deformation, can reduce or suppress the amount of twinning necessary to satisfy the imposed deformation. Therefore, shock-induced phase transition may disappear at similar stress levels but higher temperatures.

Experiment 99-0602 was carried out at a similar temperature than experiment 98-1210, but at higher velocity. The objective was to achieve complete spallation at high temperatures. For this experiment the interferometer was modified to a higher velocity per fringe, 95.1 m/s. Even though a shorter delay leg was used, the elastic precursor overcame the recording system and one fringe was added to match the boundary conditions.

According to the velocity profile shown in Fig. 12, the velocity jump corresponding to the HEL coincides with the one in experiment 98-1210 (same temperature). The plastic wave slope is larger which indicates a stronger hardening due to the larger inelastic strain rate. The unloading is dispersive and shows once again the reverse phase transformation. In between the first and second loading pulse a clear spall signal appears. Spallation occurs at a lower stress than the one reported by other investigators, e.g., Me-Bar et al. (1987). Some researchers attribute this to an incomplete fracture at the spall plane. The spall plane is shown in Fig. 13. It is known that the kinetics of damage and fracture depends on loading rate. In experiment 99-0602, the temperature of the sample favors plasticity leading to a highly ductile fracture despite the applied high strain rates.

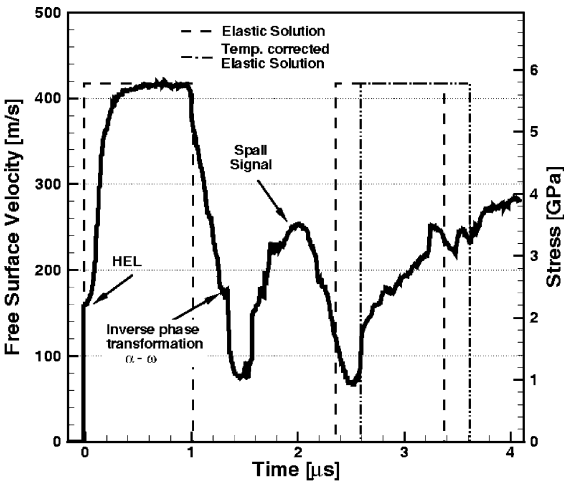

Fig. 12. Surface velocity history for experiment 99-0602, temperature 315 °C, $V_0 = 417$ m/s.

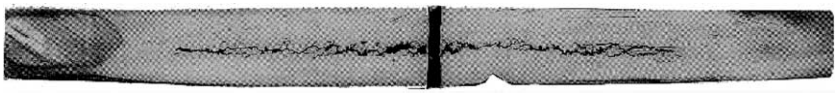

Fig. 13. Optical picture of target 99-0602. Its middle plane is partially fractured.

There are several approaches to calculate spall strength. To be consistent with results reported in the literature, for other metallic materials, the approach used by Kanel et al. (1996) is employed. Such an approach establishes the spall strength for a symmetric impact according to $0.5(\rho C)_0 \times \Delta V$, where ΔV is the velocity drop from the peak velocity to the spall signal. According to this equation, experiment 99-0602 presents a spall strength of 4.47 GPa. This value represents a reduction of about 10% from the value of 5.1 GPa, at room temperature, reported for Brar and Hopkins (1999) and Me-Bar et al. (1987). It should be noted that the tested material may have different microstructural characteristics than the material tested by Me-Bar et al. as a result of melt practice and thermomechanical treatment recipe. The reduction in spall strength with temperature has been previously reported by Kanel et al. (1996) in magnesium and aluminum. These observations are consistent with the fact that an increase in thermal activation reduces the mechanical energy required for atomic separation, enhances diffusion and phase segregation, which normally result in a reduction of cohesive strength. Furthermore, thermal stress concentration at the microstructural level usually lowers the required applied stress for nucleation of cavities. These microstructural effects manifest themselves as a decrease in macroscopic spall strength.

Oscillations in the free surface velocity profile during unloading indicates the existence of the reverse $\omega \rightarrow \alpha$ phase transition. This phase transition happens at a compressive stress level of approximately 2.25 GPa, which is slightly higher than the phase transition at room temperature.

The temperature rise in this experiment is estimated to be 40 °C, giving a final temperature of 351 °C. Like in the previous case, the final temperature is well below the β-transus.

To further explore the spall behavior, experiment 99-1008 was carried out at a temperature close to the limit of applicability of Ti–6Al–4V, i.e., about 500 °C. The impact velocity was set to about 590 m/s to ensure a complete spallation process. The velocity per fringe in the interferometer was 97.2 m/s, resulting in the loss of the elastic precursor as in experiment 98-1210. The free surface velocity profile for this last experiment is shown in Fig. 14. A consistent reduction of the HEL with temperature can be observed. The plastic wave slope is steeper than in the other discussed experiments, indicating an even stronger hardening. A Hugoniot state is clearly achieved followed by a dispersive unloading pulse as in previous experiments. The overall wave profile is smooth, indicating a progressive deformation when the wave travels through the target. In between the expected first and second loading pulses, a fast rising pull-back and clear spallation signal appears. It indicates the formation of a well-defined spall fracture plane. The high free surface velocity increase, during spallation, indicates that the fracture process is more sudden than in experiment 99-0602. In fact the recovered target was split into two pieces.

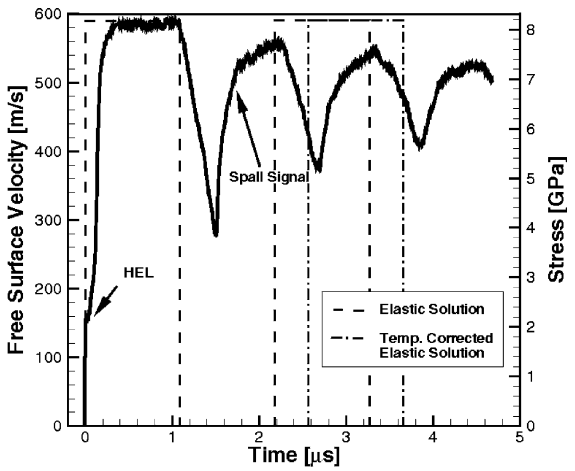

Fig. 14. Surface velocity history for experiment 99-1008, temperature 513 °C, $V_0 = 594$ m/s.

Using the approach employed by Kanel et al. (1996), the spall strength was estimated at 4.30 GPa. This indicates a reduction of 5% in the spall strength when temperature is increased from 315 to 513 °C. The decrease in spall strength is in accordance with the results reported by Kanel et al. (1996) for magnesium and aluminum.

The reverse shock phase transformation $\omega \rightarrow \alpha$ is not present in this experiment. The spall signal starts at a lower stress than the stress level required for the reverse shock transformation as previously measured. Therefore, it is not possible to conclude if the increase in peak shock stress can trigger shock transformation despite of the increase in temperature.

The reduction in cohesive forces, due to temperature, and the activation of smaller defects due to the high rate of loading may be expected to result in a significant reduction in spall strength. Nevertheless, spall strength only diminishes by half of what it diminished from room temperature to 300 °C, experiment 99-0602. One explanation could be the reduction in strain inhomogeneities resulting from thermal softening of the microstructure. Microstructural analyses of the recovered samples show that temperature reduces the amount of stress-induced damage at α–β interfaces.

The temperature rise in this experiment is estimated to be 81 °C, resulting in a final temperature of 593 °C. The final value is close to the β-transus temperature. It is known that thermomechanical properties change with allotropic transformations in Ti–6Al–4V (Shrader and Bjorkman, 1981), but our experimental results do not provide enough information to analyze such change in detail.

2.5. Microscopy analyses

The recovered specimens were analyzed with SEM microscopy in order to identify deformation mechanisms. It must be pointed out that the cooling rate of the sample after the experiment can affect the residual microstructure. Therefore, the observed microstructure may not be exactly the same as the one present at high temperature, but the damage generated by the shock-wave should remain. Another feature to be considered is that unloading waves from the periphery of the round flyer plate can cause further damage and inelasticity. The time arrival of rarefaction waves is after the VISAR signal is acquired, but could nevertheless influence the resulting microstructure to the extent that post-morten observations cannot be directly correlated to the initial shock pulse.

The recovered target plates were sectioned using a low speed diamond saw from Buehler. Then they were ground on 240, 400, 800, 1200-grit emery papers, and polished with 6 μm diamond slurry. The final polishing was carried out on a Buehler vibromet polisher using microcloth with a diamond 0.5 μm paste. Subsequently, the specimens were etched using a Kroll's reagent, 91% distilled water, 3% hydrofluoric acid (HF), and 6% of nitric acid, for 10 min. The SEM microscopy was performed using a LEO 982 with GEMINI field emission column operating at an acceleration potential of 5 kV.

In experiment 98-0924, performed at room temperature, a significant amount of microvoids, in the region of the expected spall plane, were observed, see Fig. 15. The microvoid density reaches the highest value at the expected spall plane indicating that microvoid nucleation took place during the tensile pulse. The microvoids are preferentially located at the boundaries of α grains and lamellar α–β microstructucture. It is interesting to note that most of the voids are located at triple points. The energy needed to generate these microvoids can be correlated to the observed attenuation of the second loading pulse in experiment 98-0924.

The nucleation of microvoids in two-phase alloys has been observed in quasi-static loading by several investigators, see e.g., De Meester et al. (1975). The stress–strain behavior of the phase alloys, like Ti–6Al–4V, depends on internal stresses which develop between phases to maintain plastic strains compatibility. It has been shown that under a given hydrostatic stress, void nucleation occurs as plastic instability after a certain stress threshold. Beyond this threshold, damage evolves by both continual void nucleation and linkage of voids. Helbert et al. (1998) studied the

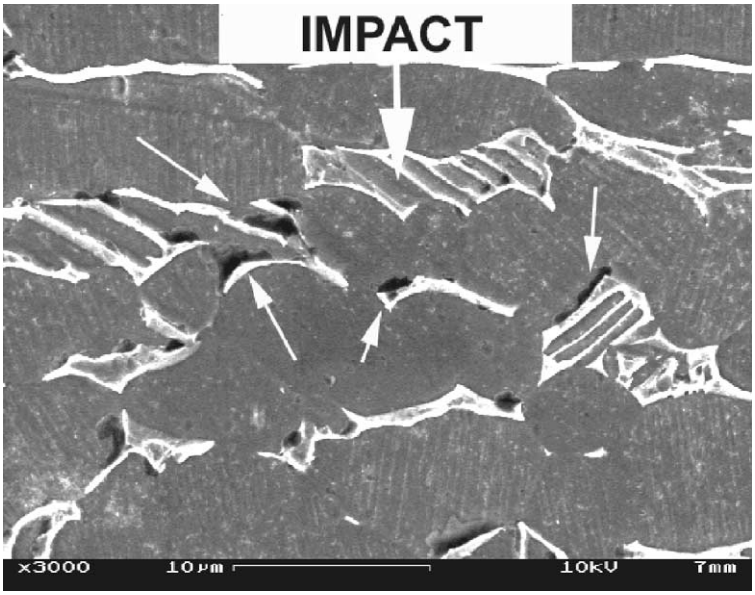

Fig. 15. SEM picture of target 98-0924, showing microvoids at α–β interfaces.

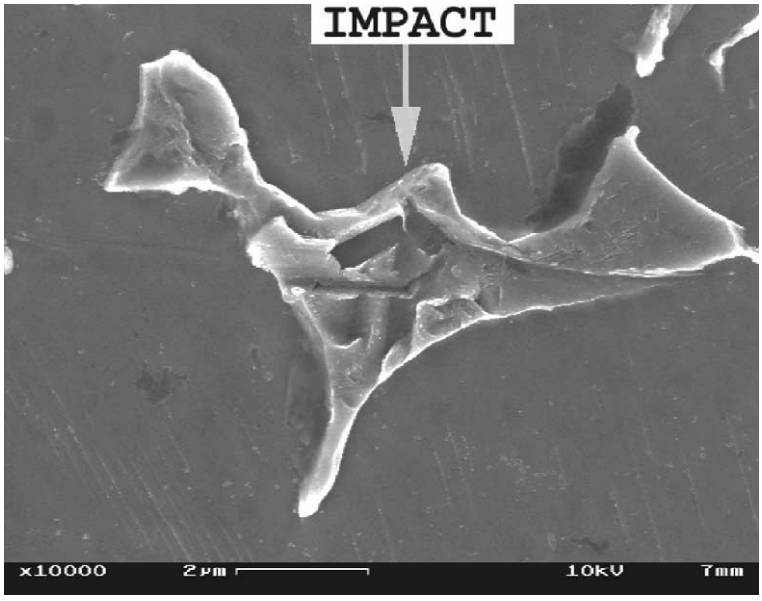

Fig. 16. Magnified view of a microvoid at a triple point.

effect of high stress triaxiality in titanium alloys. They found that plastic strain incompatibilities, arising from microstructural heterogeneities, induce significant interface stresses. These plastic strain incompatibilities reach a maximum value at triple points. Our experiments show that the same phenomenon also appears at high strain rates. A good example is shown in Fig. 16, where a

microvoid nucleate at a triple point between two α grains and a β grain.

When the sample temperature is increased, experiment 98-1210, microvoids are observed, but with several differences. There is a reduction in the size and density of microvoids. This decrease in induced damage explains the small attenuation of the second loading pulse. Another important difference is observed in Fig. 17 where it is possible to infer that most microvoids are located inside the α grains. Recalling the studies of Helbert et al. (1998), it is possible to explain the lack of microvoids at the α–α and α–β interphases. Incompatibilities in plastic strain generate high triaxiality in the stress field that leads to microvoid formation at certain locations. The increase in temperature, despite of the high strain rate, favors plastic deformation by lowering the activation barriers associated with the atomic mechanisms of deformation. Hence, the elevated temperature reduces the triaxiality of the stress field by allowing high plastic deformation to occur. Even tough plastic relaxation is enhanced by temperature, some incompatibilities can persist. Intersititial atoms can lock slip deformation and lead to high stresses *inside* the grains triggering microvoid formation. These concepts explain the small microvoids observed inside α-grains. Another interesting observation is the form of the microvoids, see Fig. 17. Under uniaxial strain, the finite deformation is restricted to the direction of impact. Therefore, once microvoids nucleate, they grow preferentially along the maximum principal stress direction, that is the impact direction. It should be noted that in this experiment the density of voids was not high enough to result in their coalescence and therefore a spall plane perpendicular to the impact direction.

Microstructural features at room temperature, in the spall region, have been studied by Me-Bar et al. (1987). It was established that voids nucleate simultaneously on the α-grain boundaries and coalesce to form well-defined fracture planes. The high temperature experiments reported in this paper present a similar behavior. Void coalescence and linkage along a plane perpendicular to the impact direction is the dominant damage mechanism. In Fig. 18, it is possible to observe that multiple damage sites, in the form of microvoids, developed in the sample and cross-linked to form the spall plane. A high magnification picture, shown in Fig. 19 puts in evidence the development

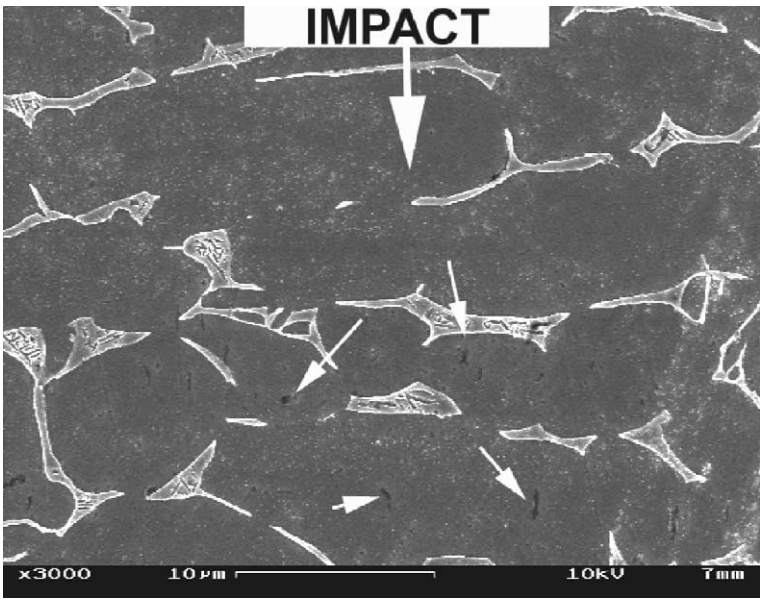

Fig. 17. Microvoid formation inside α-grains in high temperature experiment 98-1210.

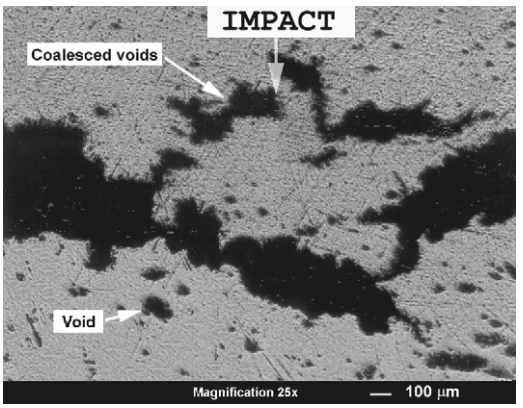

Fig. 18. Microvoid formation close to the spall plane in target 99-0602.

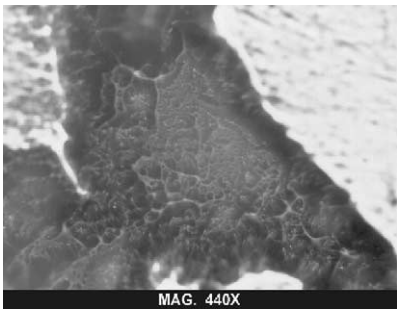

Fig. 19. High magnification optical picture of the spall fracture in target 99-0602.

of void sheets at the fracture plane. Dimpled facets and shear bridges can be clearly identified inside the ductile fracture zone.

From the fracture observations it is possible to trace the history of the failure process. Once voids have grown sufficiently to coalesce, and dimpled facets have been formed at different locations, the load is carried only by bridges between the facets. These bridges connect facets at different levels, hence the tensile stress is converted into shearing stress and the bridges fail by shearing. Even though it is possible to trace the history of the failure from a microstructural point of view, it is not possible to correlate directly the microstructural observations with the interferometer records. Numerical simulations of the experiments are needed to correlate microvoid nucleation and kinetics with the measured free surface velocity records.

3. Concluding remarks

Table 3 summarises measured dynamic properties such as HEL, spall strength and dynamic yield stress as obtained from the experimental data. A discussion of the equations employed in the calculations is given in Arrieta (1999). A summary of velocity histories is shown in Fig. 20.

Hugoniot properties of Ti–6Al–4V at high temperature are compared in Fig. 21 with the ones at room temperature obtained by Brar and Hopkins (1999). A good agreement can be noticed supporting the assumption that a stable thermodynamic state is reached during the experiments. Note that our data was corrected to account for target temperature.

It is well known that the HEL and therefore the dynamic yield stress increases with strain rate at constant temperature. Moreover, experiments performed by Lee and Lin (1998) show a drop in dynamic yield stress with temperature when the strain rate is maintained to a constant value of

Table 3
Summary of high temperature experiments

Shot no.	Preheated temperature (°C)	Strain rate (s^{-1})	Transient strain	HEL (GPa)	Dynamic yield stress (MPa)	Spall strength (GPa)
98-0924	22	1.47×10^5	0.0135	2.77	1402	5.10[a]
98-1210	298	1.61×10^5	0.0153	2.11	917	–
99-0602	315	2.27×10^5	0.0239	2.105	914	4.47
99-1008	513	3.26×10^5	0.0356	1.98	858	4.30

[a] Reported in the literature (Me-Bar et al., 1987).

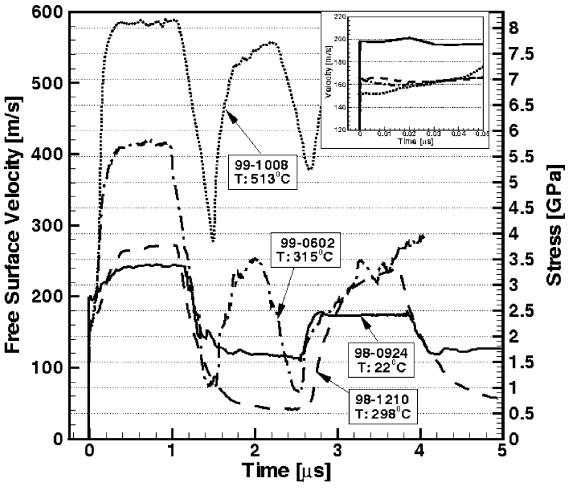

Fig. 20. Summary of velocity histories from room and high temperature experiments.

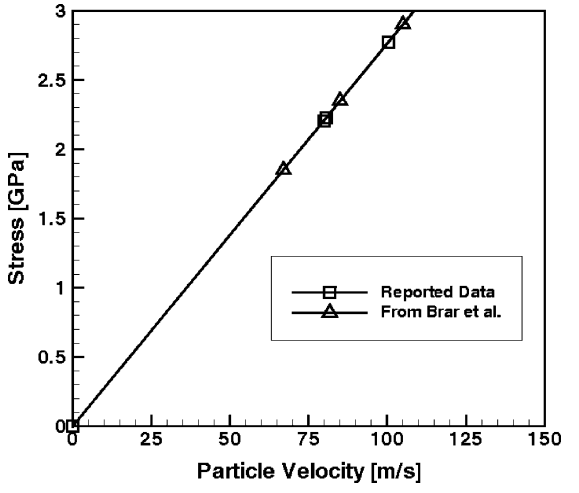

Fig. 21. $\sigma_x - U_p$ Hugoniot properties for Ti–6Al–4V.

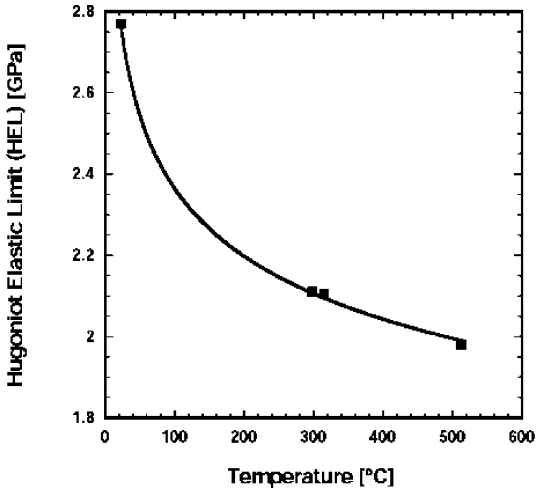

Fig. 22. Variation of HEL with temperature in Ti–6Al–4V at a strain rate of about 10^5 s^{-1}. All experimental results in this plot were obtained from the present investigation. The data points are connected by a spline, which does not correspond to any particular model.

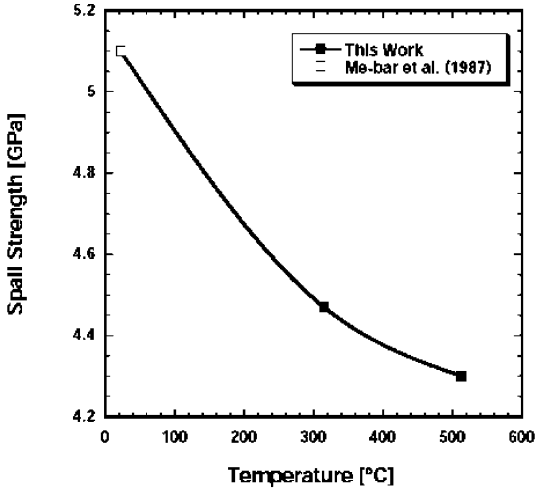

Fig. 23. Variation of the spall strength with temperature. The room temperature spall strength value is after Me-Bar et al. (1987). The data points are connected by a spline, which does not correspond to any particular model.

about 10^3 s^{-1}. The experimental results presented in this investigation show that the HEL and its associated value, the dynamic yield stress, drop significantly with temperature, when the strain rate is about 10^5 s^{-1}, see Fig. 22. This data agrees quite well with the previously cited results from Lee and Lin (1998).

From Table 3 and the data reported by Lee and Lin, it is possible to infer that both strain rate and temperature have an effect on the constitutive behavior of Ti–6Al–4V. However, the effect of strain rate, on the dynamic yield stress of Ti–6Al–4V, is secondary when compared to the effect of temperature. Thus, the rate of thermal softening prevails over the rate of work hardening under shock deformation in the elevated temperature regime.

The effect of temperature on the spall strength of Ti–6Al–4V has been observed to be similar to the one manifested on other metals, such as aluminum and magnesium (Kanel et al., 1996). The progressive reduction of spall strength with temperature is shown in Fig. 23. The measured reduction in the rate of change of the spall strength with temperature appears to be related to the increment of plastic flow favored by the increase in thermal activation. The presence of an $\alpha \rightarrow \omega$ phase transformation at approximately 2.2 GPa, may play a role in the formation of defects that promote microvoid formation and, therefore, reduction in the spall strength. The present results indicate that the spall strength reduction saturates with temperature, in a similar fashion to the dynamic properties, regardless of the presence of stress driven secondary phases.

According to our results a shock-induced phase transformation $\alpha \rightarrow \omega$ occurs at room temperature in Ti–6Al–4V when a peak stress of 3.46 GPa is achieved. The transformation is suppressed by thermal activated mechanisms at about 300 °C and 3.57 GPa. It reappears at the same temperature and a higher stress level, namely, 5.45 GPa. Therefore, temperature and strain rate play opposite roles in the generation of the $\alpha \rightarrow \omega$ shock-induced transformation in Ti–6Al–4V. A possible cause is the competition between thermally activated deformation mechanisms, such as slip, which is favored by high temperature and low strain rates, to athermal deformation mechanisms, such as twining, that is more favorable at high strain rates and stress levels.

By SEM analyses performed on the recovered samples, a correlation among the changes in wave profile with stress-induced damage on the target plates has been established. In all cases, damage in the form of microvoids has been observed. Damage at stress levels below complete spallation of the material is usually overseen. Room temperature experiment provided experimental evidence that damage at stress levels below 3.5 GPa occurs in Ti–6Al–4V, even though a pull-back signal is not present. The reported damage in Ti–6Al–4V as a function of temperature is useful for future formulations of void nucleation and growth models where the onset of inelasticity, defined as the stress threshold at which damage starts, is a relevant variable, see e.g., Curran et al. (1981). The dramatic changes in wave profile, due to thermal activation, reinforces the need for including the effect of thermal activation on deformation mechanisms in future modeling of void nucleation and growth when the material is preheated or heated by plastic deformation and/or friction.

Acknowledgements

The authors would like to thank Dr. M.G.H. Wells from the Army Research Laboratory, Aberdeen, for providing the Ti alloy used in this investigation. This research was supported by the Air Force Office of Scientific Research through Award No. F49620-98-1-0039, the Army Research Office through ARO-MURI Award No. DAAH04-96-1-0331 and the Office of Naval Research through YIP-Award No. N00014-97-1-0550.

References

Arrieta, H.V., 1999. Dynamic Fracture and Flow at High Temperatures. M.Sc. Thesis, Purdue University, West Lafayette.

Barker, L.M., 1972. Laser interferometry in shock-wave research. Exp. Mech. 12, 40.

Brar, N.S., Hopkins, A., 1999. Shock Hugoniot and shear strength of Ti–6Al–4V. In: 11th APS Topical Group Meeting on Shock Condensed Matter, Snowbird, Utah.

Campbell, J.D., 1973. High strain rate testing of aluminum. Mater. Sci. Eng. 12, 3.

Chen, G.Q., Ahrens, T.J., 1998. Radio frequency heating coils for shock wave experiments. Mater. Res. Symp. Proc. 499, 131.

Chiem, C.Y., Duffy, J., 1983. Strain rate history effects and observations of dislocation substructure in aluminum single crystals following dynamic deformation. Mater. Sci. Eng. 57 (2), 233.

Clifton, R.J., 1971. On the analysis of elastic/visco plastic waves of finite uniaxial-strain. In: Shock Waves and the Mechanical Properties of Solids. University Press, Syracuse.

Collings, E.W., Ho, J.C., 1970. Physical properties of titanium alloy. In: Science Technology and Application of Titanium. Proc. First Int. Conf. on Titanium, London. Pergamon Press, Oxford, p. 331.

Curran, D.R., Seaman, L., Shockey, D.A., 1981. In: Meyers, M.A. (Ed.), Shock Waves and High-Strain Rate Phenomena in Metals. Plenum Press, New York, p. 132.

De Meester, B., Donner, M., Conrad, H., 1975. Deformation kinetics of Ti–6Al–4V at low temperatures. Metall. Trans. A6A, 65.

Donachie, M. (Ed.), 1988. Titanium: a Technical Guide. ASM International, Metals Park, OH.

Espinosa, H.D., Clifton, R.J., 1991. Plate Impact Experiments for Investigating the Inelastic deformation and Damage of Advanced Materials. ASME Book No. H00723, pp. 37.

Espinosa, H.D., Nemat-Nasser, S., 2000. Low velocity impact experiments. In: Lampman, S. (Ed.), ASM Handbook, vol. 8.

Follansbee, P.S., Gray III, G.T., 1989. An analysis of the low temperature low and high strain rate deformation of Ti–6Al–4V. Metall. Trans. A. 20, 863.

Fowles, G.R., 1970. Gas gun for impact studies. Rev. Sci. Instr. 41, 984.

Fukuhara, M., Sanpei, A., 1993. Elastic moduli and internal frictions of Inconel 718 and Ti–6Al–4V as a function of temperature. J. Mater. Sci. Lett. 12, 1122–1124.

Frustchy, K.J., Clifton, R.J., 1998. High temperature pressure–shear plate impact experiments using tungsten carbide impactors. Exp. Mech. 58, 116.

Golubev, V.K.V., Sobolev, Y.S., 1999. Effect of temperature on spall failure of some metal alloys. In: 11th APS Topical Group Meeting on Shock Condensed Matter, Snowbird, Utah.

Gray III, G.T., 1998. Shock-induced defects in bulk materials. Mater. Res. Symp. Proc. 499, 87.

GrayIII, G.T., Morris, C.E., 1989. Deformation mechanisms in Ti–6Al–4V loaded at high strain rate. In: Lacombe, p. (Ed.), 6th World Conference in Titanium, vol. 1, pp. 269.

Helbert, A.L., Feaugas, X., Clavel, M., 1998. Effects of microstructural parameters and back stress on damage mechanisms in α–β titanium alloys. Acta Mater. 46, 939.

Hertzberg, R.W., 1996. In: Deformation and Fracture of Engineering Materials. Wiley, New York.

Hirschvogel, 1978. Metal working properties. Mech. Working Technol. 2, 61.

Johnson, W., 1979. Processes involving high strain rates. Int. Phys. Conf. Ser. 47, 337.

Kanel, G.I., Razorenov, S.V., Bogatch, A., Utkin, A.V., Fortov, V.E., 1996. Spall fracture properties of aluminum and magnesium at high temperatures. J. Appl. Phys. 79, 8310.

Kumar, P., Clifton, R.J., 1976. Optical alignment of impact faces for plate impact experiments. J. Appl. Phys. 48 (3), 1366.

Lee, W., Lin, M., 1997. The effects of strain rate and temperature on the compressive deformation behavior of Ti–6Al–4V alloy. Mater. Process. Technol. 71, 235.

Lee, W., Lin, M., 1998. Plastic flow and fracture behavior of Ti–6Al–4V alloy loaded with high strain rate under various temperatures. Mater. Sci. Eng. A241, 48.

Me-Bar, Y., Boas, M., Rosemberg, Z., 1987. Spall studies on Ti–6Al–4V. Mater. Sci. Eng. 85, 77.

Mescheryakov, Y., Divalok, A.K., Zhigacheva, N.I., 1999. Shock-induced phase transition and mechanisms of spallation in shock loaded titanium alloys. In: 11th APS Topical Group Meeting on Shock Condensed Matter, Snowbird, Utah.

Meyer, L.W., 1984. Strength and ductility of a titanium alloy Ti–6Al–4V in tensile and compressive loading under low, medium and high rates of strain. Titanium Science and Technology, Deutsche Gessellschaft Fur Metallkunde.

Nemat-Nasser, S., Guo, W., 2000. Flow stress of commertially pure niobium over a broad range of temperatures and strain rates. Mater. Sci. Eng. A, Struct. Mater. Prop. Microstruct. Process. 284 (1), 202–210.

Sakai, T., Ohashi, M., Chiba, K., 1988. Recovery and recrystallization of polycrystalline nickel after hot working. Acta Metall. 36, 1781.

Shrader, J.E., Bjorkman, M.D., 1981. High temperature phase transformation in the titanium alloy Ti–6Al–4V. In: Meyers, M.A. (Ed.), Shock Waves and High-Strain Rate Phenomena in Metal. Plenum Press, New York, p. 310.

Sikka, S.K., Vohra, Y.K., Chidambaram, R., 1982. Omega phase in materials. Prog. Mater. Sci. 27, 245.

Song, S., Gray III, G.T., 1994. Crystallographic study of α-phase in pure titanium. In: Schmidt, S.C. (Ed.), High Pres. Sc., Tech.-1993 AIP Conf., vol. 309, pp. 251.

Vohra, Y.K., Sikka, S.K., Vaidya, S.N., Chidambaram, R., 1977. Impurity effects and reaction kinetics of the pressure-induced alpha to omega transformation in Ti. J. Phys. Chem. Solids 38, 1293.

Wood, R.A., 1972. Titanium Alloy Handbook. Metals and Ceramic Center, Battelle, Publication No. MCIC-HB-02.

Yadav, S., Ramesh, K.T., 1995. The mechanical properties of tungsten-based composites at very high strain rates. Mater. Sci. Eng. A. 203, 140.

Zhou, L.X., Baker, T.N., 1994. Deformation parameters in bbc metals. Mater. Sci. Eng. A 177, 1.